

# Automatic prostate cancer detection through DCE-MRI images: all you need is a good normalization

Guillaume Lemaître<sup>a,b,\*</sup>, Robert Martí<sup>b</sup>, Mojdeh Rastgoo<sup>a</sup>, Joan Massich<sup>a</sup>,  
Jordi Freixenet<sup>b</sup>, Joan C. Vilanova<sup>c</sup>, Fabrice Meriaudeau<sup>a,d</sup>

<sup>a</sup>*LE2I UMR6306, CNRS, Arts et Métiers, Univ. Bourgogne Franche-Comté, 12 rue de la  
Fonderie, 71200 Le Creusot, France*

<sup>b</sup>*ViCOROB, Universitat de Girona, Campus Montilivi, Edifici P4, 17071 Girona, Spain*

<sup>c</sup>*Department of Magnetic Resonance, Clínica Girona, Lorenzana 36, 17002 Girona, Spain*

<sup>d</sup>*CISIR, Electrical & Electronic Engineering Department, Universiti Teknologi Petronas, 32610  
Seri Iskandar, Perak, Malaysia*

---

## Abstract

This template helps you to create a properly formatted L<sup>A</sup>T<sub>E</sub>X manuscript.

*Keywords:* DCE-MRI, prostate cancer, normalization, classification,  
quantification

---

## 1. Introduction

Prostate Cancer (PCa) is the second most frequently diagnosed men cancer,  
accounting for 899,000 cases leading to 258,100 deaths (Ferlay et al., 2010).  
As highlighted by the PI-RADS Steering Committee, the two main challenges  
5 to be addressed are (Weinreb et al., 2016): (i) the improvement of detecting  
clinically significant PCa and (ii) an increase of the confidence in benign or  
dormant cases, avoiding unnecessary invasive medical exams. In this regard,  
multiparametric Magnetic Resonance Imaging (MRI) (mp-MRI) is frequently  
used to build robust Computer-Aided Detection and Diagnosis (CAD) systems  
10 to detect, localize, and grade PCa. In general, CAD systems are based on mp-  
MRI which potentially combines several of the following modalities (Lemaître  
et al., 2015): T<sub>2</sub> Weighted (T<sub>2</sub>-W)-MRI, Dynamic Contrast-Enhanced (DCE)-

---

\*Corresponding author.

Email address: [g.lemaitre58@gmail.com](mailto:g.lemaitre58@gmail.com) (Guillaume Lemaître)

MRI, Apparent Diffusion Coefficient (ADC) maps, and Magnetic Resonance Spectroscopy Imaging (MRSI).

15     In DCE-MRI, a contrast media is injected intravenously and a set of images is acquired over time. Consequently, each voxel in an image corresponds to a dynamic signal which is related to both contrast agent concentration and the vascular properties of the tissue. Therefore, changes of the enhanced signal allows to discriminate healthy from PCa tissues. In fact, these properties are automati-  
20 cally extracted using quantitative or semi-quantitative approaches (Lemaître et al., 2015).

*Quantitative* approaches uses pharmacokinetic modelling based on a bicompart-  
ment model, namely Brix (Brix et al., 1991) and Tofts (Tofts et al., 1995) models. The parameters of the Brix model are inferred assuming a linear rela-  
25 tionship between the media concentration and the MRI signal intensity. This assumption has shown, however, to lead to inaccurately estimate the pharmacokinetic parameters (Heilmann et al., 2006). In the contrary, Tofts model requires a conversion from MRI signal intensity to concentration, which become a non-linear relationship using specific equation of MRI sequences (e.g., FLASH  
30 sequence). Tofts modelling suffers, however, from a higher complexity (Gliozzi et al., 2011). Indeed, the conversion using the non-linear approach requires to acquire a  $T_1$  map which is not always possible during clinical examination. Additionally, the parameter calculation requires the Arterial Input Function (AIF) which is challenging to measure and can also lead to inaccurate estimation.

35     *Semi-quantitative* approaches are rather mathematical than pharmacokinetic modelling since that no pharmacokinetic assumption regarding the relation between the MRI signal and the contrast agent (Huisman et al., 2001; Gliozzi et al., 2011). These methods offer the advantages to not require any knowledge about the MRI sequence nor any conversion from signal intensity to concentra-  
40 tion. However, the heuristic approach proposed by Huisman et al. requires an initial estimate of the noise standard deviation of the signal as well as manual tuning.

Nevertheless, all presented methods suffer from two major drawbacks: (i)

inter-patient variability and (ii) loss of information. The inter-patient variability  
45 is mainly due to the acquisition process and consequently leads to generalization  
issue while applying machine learning algorithm. All previous methods extract  
few discriminative parameters to describe the DCE-MRI signal which might  
lead to a loss of information.

In this work, we propose a fully automatic normalization method for DCE-  
50 MRI that reduces the inter-patient variability of the data. The benefit and  
simplicity of our approach will be shown by classifying the whole normalized  
DCE-MRI signal and comparing with the state-of-the-art quantitative and semi-  
quantitative methods. Additionally, we will show that using this normalization  
approach in conjunction with the quantitative methods improves the classifica-  
55 tion performance in for most of the models.

The benefit of our approach will be shown while using quantitative and semi-  
quantitative approaches. Additionally, we show that using the whole normalized  
DCE-MRI signal is preferable to quantitative and semi-quantitative methods,  
leading to the best classification performance.

60 The paper is organized as follows: Section 2.1 presents into details our nor-  
malization strategy for DCE-MRI data. Quantitative and semi-quantitative  
methods are summarized in Sect. 2.2 with insights about their implementations.  
Section 3 gives information about the dataset used and provided source code.  
Experiments and results to answer the previous stated challenges are reported  
65 in Sect. 4 while discussed in Sect. 5, followed by a concluding section.

## 2. Methods

### 2.1. Normalization of DCE-MRI images

In this work, we propose a method to normalize DCE-MRI prostate data  
to reduce inter-patient variations, although it can be applied to any DCE-MRI  
70 sequences. In  $T_2$ -W-MRI, these variations are characterized by a shift and  
a scaling of the intensities as illustrated by the intensity Probability Density  
Function (PDF) in Fig. 1. Therefore, these variations can be corrected using a

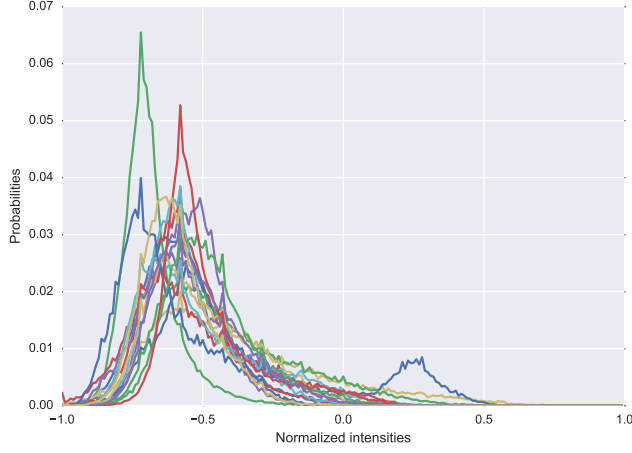


Figure 1: Illustration of the inter-patient variations in 17 different patients, using the PDF representation.

$z$ -score approach, assuming that the data follow a specific distribution (Lemaitre et al., 2016).

75 In DCE-MRI, the intensity PDF of prostate gland does not follow a unique type of distribution such as Rician or Gaussian distribution, as shown in Fig. 2(a). Indeed, the inter-patient variations are more complex due to the temporal acquisition. A better representation to observe these variations is to represent the intensity PDF of the DCE-MRI data over time using a heatmap representation  
80 as shown in Fig. 2(a). Analyzing this heatmap representation across patients (see Fig. 2(c)), the following variations are highlighted: (i) an intensity offset  $\Delta_i$  of the PDF peak at pre-contrast, (ii) a time offset  $\Delta_t$  depending of the contrast agent arrival, and (iii) a change of scale  $\sigma_i$  related to the signal enhancement. Therefore, our normalization method should attenuate all these variations and  
85 be performed globally across the different time sequence rather than for each independent sequence.

#### 2.1.1. Graph-based intensity offsets correction

Before to standardize each sequence, the first step of the normalization is to cancel the intensity specific at each patient, occurring due to the media injec-

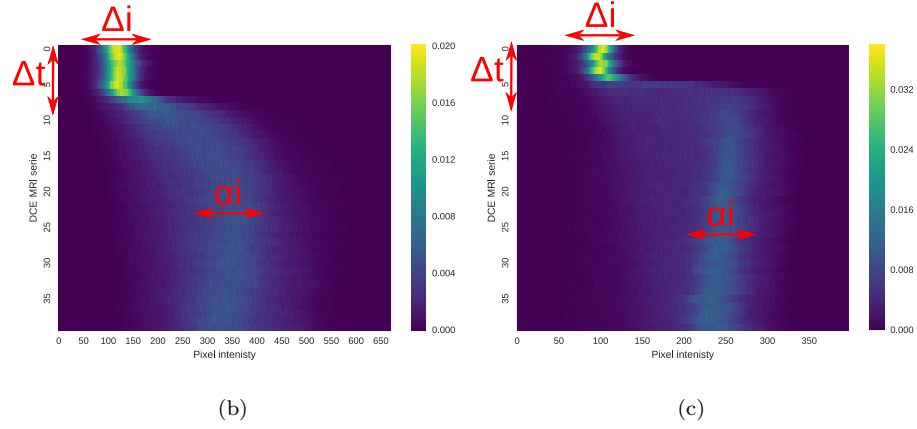
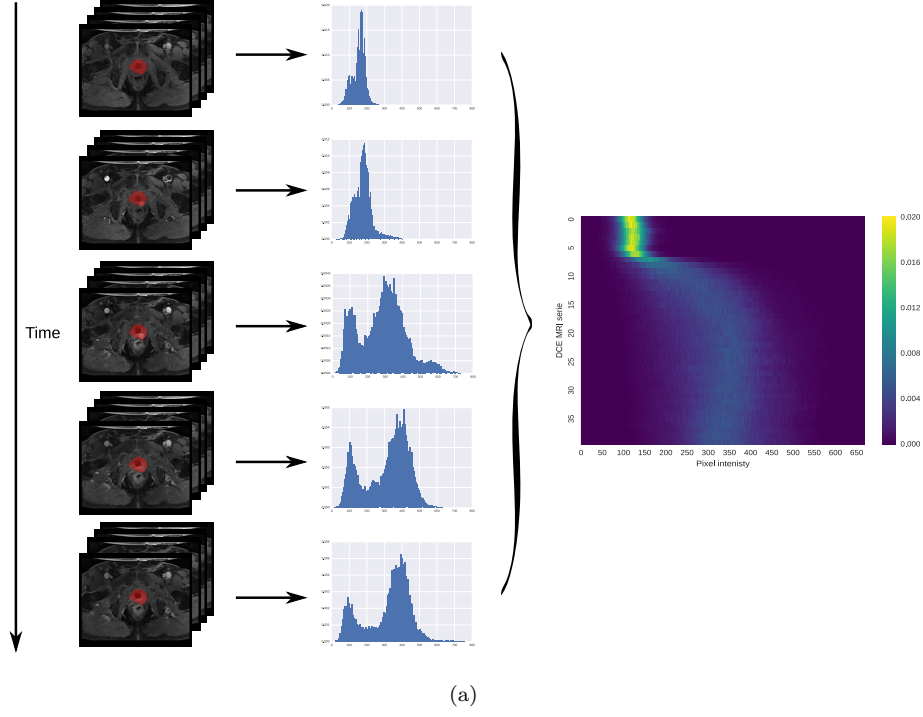


Figure 2: (a) Illustration of the heatmap representation: all PDFs of the prostate gland are concatenated together to build an heatmap; (b)-(c) Illustration of inter-patient variations (i.e.,  $\Delta_i$ ,  $\Delta_t$ , and  $\sigma_i$ ) PDF over time of two patients in a DCE-MRI.

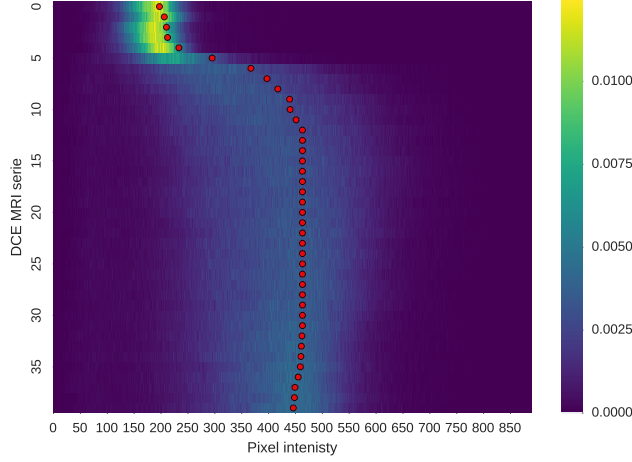
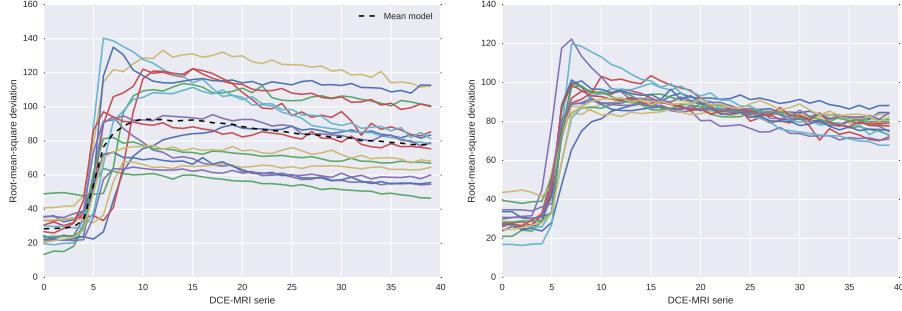


Figure 3: Illustration of the estimator found using the shortest-path through the graph.

tion. As previously mentioned, the intensity PDF does not always follow either  
a Rician or a Gaussian distribution over time, in DCE-MRI. Therefore, the  
mean of these distributions cannot be used as a potential estimate for these off-  
sets. Additionally, these offsets should be characterized by a smooth transition  
between series over time. Thus, this problem is solved using the graph-theory:  
considering the intensity PDF over time as shown in Fig. 2(a), the offsets corre-  
spond to the boundary splitting the heatmap in two partitions such that they  
are as close as possible to the peak of the intensity PDF (see Fig. 3 for an illus-  
tration). Given the heatmap, a directed weighted graph  $\mathcal{G} = (\mathcal{V}, \mathcal{E})$  is built by  
taking each bar— i.e., the probability for a given time and pixel intensity—of  
the heatmap as a node and connecting each pair of bars by an edge. The edge  
weight  $w_{ij}$  between two nodes  $i$  and  $j$  corresponding to two pixels at position  
 $(x_i, y_i)$  and  $(x_j, y_j)$ , respectively, is defined as in Eq. (1):

$$w_{ij} = \begin{cases} \alpha \exp(1 - \frac{H(i)}{\max(H)}) & \text{if } x_j = x_i + 1 \text{ and } y_j = y_i, \\ (1 - \alpha) \exp(1 - \frac{H(i)}{\max(H)}) & \text{if } x_j = x_i \text{ and } y_j = y_i + 1, \\ 0 & \text{otherwise,} \end{cases} \quad (1)$$

where  $H$  is the heatmap,  $\alpha$  is a smoothing parameter controlling the partition-



(a) RMSD computed for each patient of our dataset. (b) RMSD after alignment using the curve parametric model.

Figure 4: Illustration of the correction of the time offset and the data dispersion.

ing.

Therefore, these offsets are estimated by finding the shortest-path to cross the graph using Dijkstra’s algorithm. The entry and exiting nodes are set to be the bin with the maximum probability for the first DCE-MRI serie and the bin corresponding to the median value for the last DCE-MRI serie, respectively. To ensure a robust estimation of these offsets, the process of finding the shortest-path is iteratively repeated by shifting the data and updating the heatmap as well as the graph  $\mathcal{G}$ . The procedure is stopped once that the offset found does not change. In general, this process is not repeated more than 3 iterations. Figure 3 illustrates the final estimation of the offsets (i.e., red landmark) found for each DCE-MRI serie. Therefore, each intensity offset is subtracted for each DCE-MRI.

### 2.1.2. Time offset and data dispersion correction

The next variations to correct are the time offset and the data dispersion. By computing the Root-Mean-Square Deviation (RMSD) of the intensities for each DCE-MRI serie, one can observe these two variations as shown in Fig. 4(a). Therefore, to correct these variations, we propose to register each patient RMSD to a mean model which corresponds to the mean of all patients RMSD. The

parametric model to perform the registration is formulated as in Eq. (2):

$$T(\alpha, \tau, f(t)) = \alpha f(t - \tau), \quad (2)$$

where  $\alpha$  and  $\tau$  are the two parameters handling the time offset and global scale, respectively,  $f(\cdot)$  is the RMSD function define as:

$$f(t) = \sqrt{\left( \frac{\sum_{n=0}^N x(t)_n^2}{N} \right)}, \quad (3)$$

125 where  $x(t)_n$  is the shifted intensity of a sample from a specific DCE-MRI serie at time  $t$  from a total number of  $N$  samples.

Therefore the registration problem is equivalent to:

$$\arg \min_{\alpha, \tau} = \sum_{t=0}^N [T(\alpha, \tau, f(t)) - \mu(t)]^2, \quad (4)$$

where  $\mu(\cdot)$  is the mean model,  $N$  is the number of DCE-MRI serie.

130 Illustration of the correction applied to each RMSD patient is shown in Fig. 4(b). Once all these parameters have been inferred, the data are shifted as well as scale.

The resulting normalized data can be classified into two fashions: (i) each normalized signal can be classified considering the whole DCE-MRI signal or (ii) the normalized data can be fitted using a quantitative method, as presented 135 in the next section. However, in the second strategy, this is necessary to apply common intensity offsets such that the data follow a shape as expected by the different quantitative models. The set of offsets applied is in fact corresponding to the maximum offsets found in Sect. 2.1.1.

## 2.2. Quantification of DCE-MRI

140 In this section, we summarize the different methods which have been used for the quantification of DCE-MRI for PCa detection (Lemaître et al., 2015) and which will be used for comparison in this work. Furthermore, we would like to emphasize the following additional contributions: (i) a novel automatic AIF



estimation algorithm based on clustering and (ii) a simplified semi-quantitative  
 145 method using constrained optimization.

### 2.2.1. Brix and Hoffmann models

In the Brix model (Brix et al., 1991), the MRI signal intensity is assumed to be proportional to the media concentration. Therefore, the model is expressed as in Eq. (5):

$$s_n(t) = 1 + A \left[ \frac{\exp(k_{el}t') - 1}{k_{ep}(k_{ep} - k_{el})} \exp(-k_{el}t) - \frac{\exp(k_{ep}t') - 1}{k_{el}(k_{ep} - k_{el})} \exp(-k_{ep}t) \right], \quad (5)$$

150 with

$$s_n(t) = \frac{s(t)}{S_0}, \quad (6)$$

where  $s(t)$  and  $S_0$  are the MRI signal intensity at time  $t$  and the average pre-contrast MRI signal intensity, respectively;  $A$ ,  $k_{el}$ , and  $k_{ep}$  are the constant proportional to the transfer constant, the diffusion rate constant, and the rate constant, respectively. Additionally,  $t'$  is set such that  $0 \leq t \leq \tau$ ,  $t' = t$  and  
 155 afterwards while  $t > \tau$ ,  $t' = \tau$ .

Hoffmann et al. proposed a similar model as expressed in Eq. (7), which derive from the Brix model:

$$s_n(t) = 1 + \frac{A}{\tau} \left[ \frac{k_{ep}(\exp(k_{el}t') - 1)}{k_{el}(k_{ep} - k_{el})} \exp(-k_{el}t) - \frac{\exp(k_{ep}t') - 1}{(k_{ep} - k_{el})} \exp(-k_{ep}t) \right], \quad (7)$$

in which the constant  $A$  is redefined by isolating the parameter  $\tau$ .

The parameters  $A$ ,  $k_{el}$ , and  $k_{ep}$  are estimated by fitting the model using  
 160 non-linear least-squares optimization solved with Levenberg-Marquardt.

### 2.2.2. Tofts model

The extended Tofts model is formulated as in Eq. (8):

$$C_t(t) = K_{trans}C_p(t) * \exp(-k_{ep}t) + v_p C_p(t), \quad (8)$$

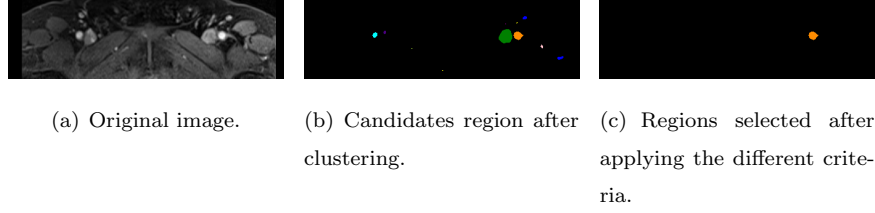


Figure 5: Illustration of the segmentation of the area used to determine the AIF.

where  $*$  is the convolution operator;  $C_t(t)$  and  $C_p(t)$  is the concentration of contrast agent in the tissue and in the plasma, respectively;  $K_{trans}$ ,  $k_{ep}$ , and  $v_p$  are the volume transfer constant, the diffusion rate constant, and the plasma volume fraction, respectively.

Therefore, Tofts model requires to: (i) detect candidate voxels from the femoral or iliac arteries and estimate a patient-based AIF signal, (ii) convert the MRI signal intensity (i.e., AIF and dynamic signal) to a concentration, and (iii) in the case of a population-based AIF, estimate an AIF signal.

#### Segmentation of artery voxels and patient-based AIF estimation

The AIF signal from DCE-MRI can be manually estimated by selecting the most-enhanced voxels from the femoral or iliac arteries (Meng et al., 2010). Few methods have been proposed to address the automated extraction of AIF signal. Chen et al. filtered successively the possible candidates to be considered as AIF such that (Chen et al., 2008): (i) dynamic signals with small peak and voxels with a small wash-in are rejected by thresholding, (ii) a blob detector is used and large enough regions are kept, and (iii) circular and cylindricity criteria are used to reject the last false positive. Zhu et al. proposed an iterative method selecting voxels which best fit a gamma variate function (Zhu et al., 2011). However, it requires to compute first and second derivatives as well as maximum curvature points. Shanbhag et al. proposed a 4-steps algorithm (Shanbhag et al., 2012; Fennessy et al., 2015): (i) remove slices with artefacts and find the best slices based on intrinsic anatomic landmarks and enhancement characteristics,

(ii) find the voxel candidates using the maximum enhanced voxels and a multi-label maximum entropy based thresholding algorithm, (iii) exclude region next to the endorectal coil, and (iv) select the best 5 candidates which meet enhancement characteristics and that are correlated.

190 All the above methods are rather complex and thus we propose a method which is based on the following simple assumptions: (i) all possible AIF signal candidates should have a similar shape, (ii) an high enhancement, and (iii) the arteries should be almost round and within a size range. Therefore, each slice is clustered into regions using K-means clustering  
195 with  $k = 6$ . The cluster with the highest enhancement—i.e. corresponding to the 90<sup>th</sup> percentile of the maximum of each dynamic signal—contain the arteries and is selected. Finally, regions with an eccentricity smaller than 0.5 and an area in the range of  $[100, 400]$  voxels are kept. Additionally, to remove voxels contaminated by partial volume effect, only the 10%  
200 most enhanced voxels of the possible candidates are kept as proposed by (Schabel and Parker, 2008) and the average signal is computed. A summary of the different segmentation steps is presented in Fig. 5.

**Conversion of MRI signal intensity to concentration** To estimate the free parameters of the Tofts model (see Eq. (8)), the concentration  $C_t(t)$  and  $C_p(t)$  need to be computed from the MRI signal intensity and the AIF signal, respectively. This conversion is based on the equation of the FLASH sequence—see Appendix A for details—and is formulated as in Eq. (9):

$$c(t) = \frac{1}{TR \cdot r_1} \ln \left( \frac{1 - \cos \alpha \cdot S^* \frac{s(t)}{S_0}}{1 - S^* \frac{s(t)}{S_0}} \right) - \frac{R_{10}}{r_1}, \quad (9)$$

with,

$$S^* = \frac{1 - \exp(-TR \cdot R_{10})}{1 - \cos \alpha \cdot \exp(-TR \cdot R_{10})}, \quad (10)$$

where  $s(t)$  is the MRI signal,  $S_0$  is the MRI signal prior to the injection of the contrast media,  $\alpha$  is the flip angle,  $TR$  is the Repetition Time (TR),  
205  $R_{10}$  is the pre-contrast tissue relaxation time also equal to  $\frac{1}{T_{10}}$ ,  $r_1$  is the relaxitivity coefficient of the contrast agent.

210  $T_{10}$  can be estimated from the acquisition of a  $T_1$  map. However, this modality is not part of the clinical trial in this research and the value of  $T_{10}$  is fixed to 1600 ms for both blood and prostate, in accordance with the values found in the literature (Fennessy et al., 2015; De Bazelaire et al., 2004; Carr and Carroll, 2011).

**Estimation of population-based AIF** While estimating the pharmacokinetic parameters from Tofts model, the AIF concentration  $C_p(t)$  can be computed either from the patient or a population. We presented in the two previous sections the algorithms which allows to estimate the patient-based AIF concentration. To compare with the previous approach, we also computed a population-based AIF which will be also used later to compare the performance of both approaches. In that regard, the population-based AIF was estimated as in (Meng et al., 2010) by fitting the average patient-based AIFs to the model of Parker et al. (2006) which is formulated as in Eq. (11):

$$C_p(t) = \sum_{n=1}^2 \frac{A_n}{\sigma_n \sqrt{2\pi}} \exp\left(\frac{-(t - T_n)^2}{2\sigma_n^2}\right) + \frac{\alpha \exp(-\beta t)}{1 + \exp(-s(t - \tau))}, \quad (11)$$

215 where  $A_n$ ,  $T_n$ , and  $\sigma_n$  are the scaling constants, centers, and widths of the  $n^{\text{th}}$  Gaussian,  $\alpha$  and  $\beta$  are the amplitude and decay constant of the exponential; and  $s$  and  $\tau$  are the width and center of the sigmoid function, respectively.

The parameters are estimated by fitting the model using non-linear least-squares optimization solved with Levenberg-Marcquardt.

### 2.2.3. PUN model

220 Gliozzi et al. showed that Phenomenological Universalities (PUN) approach can be used for DCE-MRI analysis (Gliozzi et al., 2011). The model has been successfully used in a CAD system proposed by Giannini et al. (2015). This

model can be expressed as in Eq. (12):

$$s_n(t) = \exp \left[ rt + \frac{1}{\beta} (a_0 - r) (\exp(\beta t) - 1) \right], \quad (12)$$

with

$$s_n(t) = \frac{s(t) - S_0}{S_0}, \quad (13)$$

where  $s(t)$  and  $S_0$  are the MRI signal intensity at time  $t$  and the average pre-contrast MRI signal intensity, respectively;  $r$ ,  $a_0$ , and  $\beta$  are the free parameters of the model.

The parameters are estimated by fitting the model using non-linear least-squares optimization solved with Levenberg-Marcquardt.

#### 2.2.4. Semi-quantitative analysis

The semi-quantitative analysis of the DCE-MRI is equivalent to extracting curve characteristics directly from the signal without a strict theoretical pharmacokinetic meaning. In this work, we use the model presented by Huisman et al. (2001) which formulated the MRI signal as in Eq. (14):

$$s(t) = \begin{cases} S_0 & 0 \leq t \leq t_0 \\ S_M - (S_M - S_0) \exp\left(\frac{-(t-t_0)}{\tau}\right) & t_0 < t \leq t_0 + 2\tau \\ S_M - (S_M - S_0) \exp\left(\frac{-(t-t_0)}{\tau}\right) + w(t - t_0 + 2\tau) & t > t_0 + 2\tau \end{cases} \quad (14)$$

where  $s(t)$  is the MRI signal intensity,  $S_0$  is the pre-contrast signal intensity,  $t_0$  is the time corresponding to the start of enhancement,  $S_M$  and  $\tau$  is the maximum of the signal and the exponential time constant, and  $w$  is the slope of the linear part.

Huisman et al. argue that curve fitting via least-squares minimization using Nelder-Mead algorithm leads to inaccurate estimation of the free parameters: mainly the issue come from an incorrect estimation of the start of enhancement  $t_0$  leading to incorrect estimation of the other parameters. Therefore, they

propose to: (i) estimate robustly  $t_0$ , (ii) estimate  $S_0$  by averaging the samples between 0 and  $t_0$  (ii) estimate  $w$  depending if the slope is significant or not, (iii) estimate  $S_M$  which should be the point at the intersection of the most probable  
245 slope line and the plateau.

Instead of these successive estimations, we propose a unified optimization in which  $t_0$  is fixed since that this is a key parameter. Therefore,  $t_0$  is robustly estimated from the AIF signal since that this is the most enhanced signal in which the start of enhancement is easily identifiable. The AIF signal is computed  
250 as in Section 2.2.2.  $t_0$  is estimated by finding the maximum of the first derivative of the AIF signal, always occurring at the beginning of the signal. Then, the function in Eq. (14) is fitted using non-linear least squares with Trust Region Reflective algorithm (Sorensen, 1982). Furthermore, the parameters  $\tau$  and  $S_M$  are bounded during the optimization to ensure robust estimations.  $\tau$  is bounded  
255 between  $t_0$  and  $t_f$  which is the time of the last sample while  $S_M$  is bounded between  $S_0$  and  $\max(s(t))$ .

From Eq. (14), the following features are extracted: (i) the wash-in corresponding to the slope between  $t_0$  and  $t_0 + 2\tau$ , (ii) the wash-out corresponding to the parameter  $w$ , (iii) the area under the curve between  $t_0$  and the end of the  
260 signal, (iv) the exponential time constant  $\tau$ , and (v) the relative enhancement  $S_M - S_0$ .

### 3. Materials

#### 3.1. Data

The multi-parametric MRI data are acquired from a cohort of patients with  
265 higher-than-normal level of Prostate-Specific Antigen (PSA). The acquisition is performed using a 3T whole body MRI scanner (Siemens Magnetom Trio TIM, Erlangen, Germany) using sequences to obtain T<sub>2</sub>-W-MRI, DCE-MRI and Diffusion Weighted (DW)-MRI. Aside of the MRI examination, these patients also have underwent a guided-biopsy. The dataset is composed of a total of  
270 20 patients of which 18 patients have biopsy proven PCa and 2 patients are

“healthy” with negative biopsies. Therefore, 13 patients have a PCa in the Peripheral Zone (PZ), 3 patients have PCa in the Central Gland (CG), 2 patients have invasive PCa in both PZ and CG and finally 2 patients are considered as “healthy”. An experienced radiologist has segmented the prostate organ — on  
275 T<sub>2</sub>-W-MRI and DCE-MRI — as well as the prostate zones (i.e., PZ and CG) and PCa on the T<sub>2</sub>-W-MRI.

A 3 mm slice fat-suppressed T<sub>2</sub>-W fast spin-echo sequence (TR/Echo Time (TE)/Echo Train Length (ETL): 3400 ms/85 ms/13) is used to acquire images in sagittal and oblique coronal planes, the latter planes being orientated perpendicular or parallel to the prostate PZ rectal wall axis. Three-dimensional T<sub>2</sub>-W  
280 fast spin-echo (TR/TE/ETL: 3600 ms/143 ms/109, slice thickness: 1.25 mm) images are then acquired in an oblique axial plane. The nominal matrix and Field Of View (FOV) of the 3D T<sub>2</sub>-W fast spin-echo images are  $320 \times 256$  and  $280 \times 240$  mm<sup>2</sup>, respectively, thereby affording sub-millimetric pixel resolution  
285 within the imaging plane.

DCE-MRI is performed using a fat suppressed 3D T<sub>1</sub> VIBE sequence (TR/TE/Flip angle: 3.25 ms/1.12 ms/10°; Matrix:  $256 \times 192$ ; FOV:  $280 \times 210$  (with 75% rectangular FOV); slab of 16 partitions of 3.5 mm thickness; temporal resolution: 6 s/slab over approximately 5 min). A power injector (Medrad, Indianola, USA)  
290 is used to provide a bolus injection of Gd-DTPA (Dotarem, Guerbet, Roissy, France) at a dose of 0.2 ml Gd-DTPA/kg of body weight.

These DCE-MRI sequences are resampled using the spatial information of the T<sub>2</sub>-W-MRI and missing data are interpolated using a linear interpolation. The volumes of the DCE-MRI dynamic are rigidly registered, to remove any  
295 patient motion during the acquisition. Furthermore, a non-rigid registration is performed between the T<sub>2</sub>-W-MRI and DCE-MRI in order to propagate the prostate zones and PCa ground-truths. The resampling is implemented in C++ using the Insight Segmentation and Registration Toolkit (Ibanez et al., 2005).

Table 1: Coefficient of determination  $R^2$  (i.e.,  $\mu (\pm\sigma)$ ), while fitting data with the different quantification models.

Data type	Brix	Hoffmann	Tofts population AIF	Tofts patient AIF	PUN	Semi-quantitative
Un-normalized	0.85 ( $\pm 0.11$ )	0.81 ( $\pm 0.17$ )	0.84 ( $\pm 0.14$ )	0.88 ( $\pm 0.12$ )	0.27 ( $\pm 0.18$ )	0.64 ( $\pm 0.24$ )
Normalized	0.92 ( $\pm 0.05$ )	0.72 ( $\pm 0.32$ )	0.92 ( $\pm 0.06$ )	0.90 ( $\pm 0.10$ )	0.28 ( $\pm 0.20$ )	0.75 ( $\pm 0.20$ )

### 3.2. Implementation

300 The implementation of the registration (C++), normalization (Python), and classification pipeline (Python) are publicly available on GitHub<sup>1</sup>. The data used for this work are also publicly available<sup>2</sup>.

## 4. Experiments and results

### 4.1. Goodness of model fitting

305 Parameter estimation of the quantification methods are related to fit a specific model to the DCE-MRI data. Therefore, this section report the goodness of fitting by computing the coefficient of determination  $R^2$  such as in Eq. (15)

$$R^2 = 1 - \frac{\sum_{t=0}^T (s_t - \hat{s}_t)^2}{\sum_{t=0}^T (s_t - \bar{s})^2}, \quad (15)$$

where  $s_t$  and  $\hat{s}_t$  are the signal to be fitted and the estimated signal at time  $t$ , respectively;  $\bar{s}$  is the average signal to be fitted.

310 Mean and standard-deviation of the coefficient of determination  $R^2$  is reported in Table 1 for each quantification model. Brix, Hoffmann, and Tofts models are fitted with a coefficient  $R^2$  superior to 0.80. Additionally, the proposed PUN model does not seem to fit well the data. Normalizing the data improve the coefficient  $R^2$  for all the methods apart of the Hoffmann model.  
315 The large standard deviation for this model might imply that there is some cases, that the fitting fails.



Table 2: AUC for each individual pharmacokinetic parameter using a RF classifier.

Features	Un-normalized data	Normalized data
<b>Brix model</b>		
$A$	0.54	0.55
$k_{el}$	0.51	0.50
$k_{ep}$	0.55	0.58
<b>Hoffmann model</b>		
$A$	0.52	0.51
$k_{el}$	0.55	0.53
$k_{ep}$	0.55	0.54
<b>Tofts model with population AIF</b>		
$K_{trans}$	0.56	0.55
$v_e$	0.49	0.49
$v_p$	0.53	0.50
<b>Tofts model with patient AIF</b>		
$K_{trans}$	0.57	0.57
$v_e$	0.51	0.53
$v_p$	0.53	0.55
<b>PUN model</b>		
$a_0$	0.52	0.53
$r$	0.55	0.57
$\beta$	0.53	0.55
<b>Semi-quantitative analysis</b>		
wash-in	0.57	0.53
wash-out	0.52	0.49
IAUC	0.51	0.51
$\tau$	0.57	0.54
$S_M - S_0$	0.56	0.53

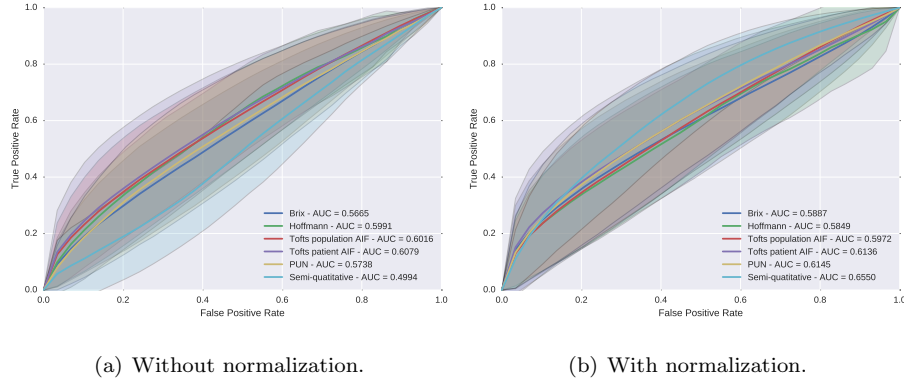


Figure 6: ROC analysis using a RF classifier with and without normalization DCE-MRI data for different pharmacokinetic models.

#### 4.2. Detection of PCa using pharmacokinetic parameters

To study the potential benefit of our normalization, PCa are detected using pharmacokinetic parameters estimated from un-normalized and normalized DCE-MRI data. Each individual pharmacokinetic parameter is classified to evaluate their individual discriminative power to detect PCa. Therefore, a Random Forest (RF) classifier is used in conjunction with a Leave-One-Patient-Out Cross-Validation (LOPO CV). The use of RF is motivated since that it leads to the best performance in the state-of-the-art methods (Litjens et al., 2014; Lemaître et al., 2015). Results are summarized in Table 2 in terms of Area Under the Curve (AUC). Normalization can improve the detection of PCa; however, the benefit of normalization is more obvious by combining the pharmacokinetic features of each model, as previously done in traditional CAD system (Lemaître et al., 2015). For the latter configuration, results are summarized by performing a Receiver Operating Characteristic (ROC) analysis and computing the AUC, as reported in Fig. 6. Quantification using normalized data outperforms quantification using un-normalized data in terms of classification performance apart

<sup>1</sup><https://github.com/I2Cvb/lemaitre-2016-nov/tree/master>

<sup>2</sup><http://kaggle.com>

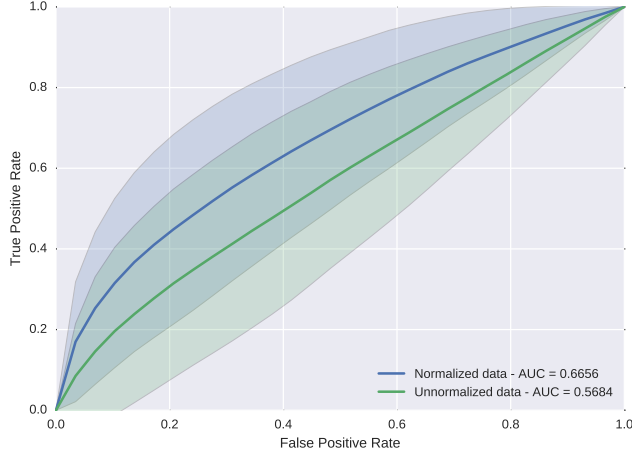


Figure 7: ROC analysis using the entire DCE-MRI signal with and without normalization in conjunction with a RF classifier.

of Hoffmann and Tofts population-based AIF models. The reasons behind the decrease of the AUC might be related to: (i) a poor fitting as discussed in Sect. 4.1 (cf., Hoffmann model) and (ii) a small number of patient while estimating some parameters (cf., Tofts model). The best classification performance are obtained using the semi-quantitative approach with an AUC of 0.655.

#### 4.3. Classification of the entire enhanced DCE-MRI signal

As stated in the introduction, the quantification methods are extracting a set of parameters characterizing the enhancement DCE-MRI signal. However, this extraction might lead to a loss of information. This experiment is performed to assess if making use of the whole DCE-MRI signal instead of the just the pharmacokinetic parameters can improve the classification performance. Therefore, each enhanced DCE-MRI signal, normalized and un-normalized, is classified using a RF classifier in a LOPO CV fashion. The ROC analysis and AUC are reported in Fig. 7. Classification without normalization lead to the worst performance, with an AUC of 0.568. However, data normalization in conjunction with the use of the whole DCE-MRI signal is the strategy which outperforms all others, with an AUC of 0.666.

## 350 5. Discussions

The experiments conducted in the previous section can give rise to several discussions. In Tofts quantification, two different approaches have been used to infer the pharmacokinetic parameters: using a population-based or a patient-based AIF. The patient-based AIF approach leads to better classification performance. However, there is two shortcomings to take into account while advancing this fact: (i)  $T_{10}$  parameter has been fixed and not computed from a  $T_1$  map and (ii) the population-based AIF has been estimated from a cohort of only 17 patients. These two limitations have to be considered while advancing that population-based AIF modelling is outperforming patient-based AIF modelling.

The best classification performance is reached by normalizing the DCE-MRI data and use the whole enhanced signal as feature, emphasizing the fact that a loss of information while extracting quantitative parameters. Furthermore, this normalization is a less complex process than all quantification methods. However, this strategy suffers from one drawback: the training time of the RF classifier increases since that from 3 to 5 features, the feature space become a 40 dimensions space.

## 6. Conclusions and future works

In this work, we presented a new method for normalizing/standardizing DCE-MRI data. This method aimed at reducing the inter-patient variations occurring during data acquisition. A graph-based approach was used to correct intensity offset in conjunction with a model-based correction to reduce time offset as well as intensity scaling. We show the benefit of our normalization method prior to extract quantitative and semi-quantitative features, with a significant improvement of the classification performance. Nevertheless, we also show that using the whole normalized DCE-MRI signal outperforms all quantitative approach.

As avenues for future research, this normalization has to be part of a mp-MRI CAD system in which DCE-MRI modality needs to be combined with  
 380 other complementary modalities.

## Appendix A. Conversion from FLASH signal to media concentration

In this appendix, we show the demonstration used to extract the agent concentration from the MRI signal.

The signal equation in FLASH sequence (Haase et al., 1986) is defined as:

$$s(t) = S_{eq} \sin \alpha \cdot \frac{1 - \exp(-TR(R_{10} + r_1 c(t)))}{1 - \cos \alpha \cdot \exp(-TR(R_{10} + r_1 c(t)))}, \quad (\text{A.1})$$

385 where  $s(t)$  is the MRI signal,  $S_{eq}$  is the maximum signal amplitude of the spoiled gradient at the TE which is proportional to the Proton Density (PD),  $\alpha$  is the flip angle,  $TR$  is the Repetition Time (TR),  $R_{10}$  is the pre-contrast tissue relaxation time also equal to  $\frac{1}{T_{10}}$ ,  $r_1$  is the relaxivity coefficient of the contrast agent, and  $c(t)$  is the media concentration.

390 Therefore, the pre-contrast signal prior to bolus injection of the media is defined as:

$$S_0 = S_{eq} \sin \alpha \cdot \frac{1 - \exp(-TR \cdot R_{10})}{1 - \cos \alpha \cdot \exp(-TR \cdot R_{10})}. \quad (\text{A.2})$$

To simplify the demonstration, let us define:

$$A = \exp(-TR \cdot R_{10}), \quad (\text{A.3})$$

$$B = \exp(-TR \cdot r_1 c(t)). \quad (\text{A.4})$$

Let us define:

$$S^* = \frac{S_0}{S_{eq} \sin \alpha}, \quad (\text{A.5})$$

$$= \frac{1 - A}{1 - A \cos \alpha}. \quad (\text{A.6})$$

Thus,

$$S^* \frac{s(t)}{S_0} = \frac{S_0}{S_{eq} \sin \alpha} \frac{s(t)}{S_0}, \quad (\text{A.7})$$

$$= \frac{1 - AB}{1 - AB \cos \alpha}. \quad (\text{A.8})$$

395 Now, let us define:

$$\frac{1 - \cos \alpha \cdot S^* \frac{s(t)}{S_0}}{1 - S^* \frac{s(t)}{S_0}} = \frac{1 - \cos \alpha \left( \frac{1-AB}{1-AB \cos \alpha} \right)}{1 - \frac{1-AB}{1-AB \cos \alpha}}, \quad (\text{A.9})$$

$$= \frac{1 - AB \cos \alpha - \cos \alpha (1 - AB)}{1 - AB \cos \alpha - (1 - AB)}, \quad (\text{A.10})$$

$$= \frac{1 - AB \cos \alpha - \cos \alpha + AB \cos \alpha}{1 - AB \cos \alpha - 1 + AB}, \quad (\text{A.11})$$

$$= \frac{1 - \cos \alpha}{AB(1 - \cos \alpha)}, \quad (\text{A.12})$$

$$= \frac{1}{AB}. \quad (\text{A.13})$$

Thus,

$$-TR \cdot R_{10} - TR \cdot r_1 c(t) = \ln \left( \frac{1 - \cos \alpha \cdot S^* \frac{s(t)}{S_0}}{1 - S^* \frac{s(t)}{S_0}} \right). \quad (\text{A.14})$$

Therefore,

$$c(t) = \frac{1}{TR \cdot r_1} \ln \left( \frac{1 - \cos \alpha \cdot S^* \frac{s(t)}{S_0}}{1 - S^* \frac{s(t)}{S_0}} \right) - \frac{R_{10}}{r_1}. \quad (\text{A.15})$$

## References

- Brix, G., Semmler, W., Port, R., Schad, L.R., Lauer, G., Lorenz, W.J., 1991. Pharmacokinetic parameters in cns gd-dtpa enhanced mr imaging. Journal of computer assisted tomography 15, 621–628.
- 400 Carr, J.C., Carroll, T.J., 2011. Magnetic resonance angiography: principles and applications. Springer Science & Business Media.

- Chen, J., Yao, J., Thomasson, D., 2008. Automatic determination of arterial  
405 input function for dynamic contrast enhanced mri in tumor assessment, in: International Conference on Medical Image Computing and Computer-Assisted Intervention, Springer. pp. 594–601. doi:10.1007/978-3-540-85988-8\_71.
- De Bazelaire, C.M., Duhamel, G.D., Rofsky, N.M., Alsop, D.C., 2004. Mr  
imaging relaxation times of abdominal and pelvic tissues measured in vivo at  
410 3.0 t: preliminary results 1. Radiology 230, 652–659. doi:10.1148/radiol.2303021331.
- Fennessy, F.M., Fedorov, A., Penzkofer, T., Kim, K.W., Hirsch, M.S., Vangel,  
M.G., Masry, P., Flood, T.A., Chang, M.C., Tempany, C.M., et al., 2015.  
Quantitative pharmacokinetic analysis of prostate cancer dce-mri at 3t: com-  
415 parison of two arterial input functions on cancer detection with digitized whole  
mount histopathological validation. Magnetic resonance imaging 33, 886–894.  
doi:10.1016/j.mri.2015.02.008.
- Ferlay, J., Shin, H.R., Bray, F., Forman, D., Mathers, C., Parkin, D.M., 2010.  
Estimates of worldwide burden of cancer in 2008: Globocan 2008. Interna-  
420 tional journal of cancer 127, 2893–2917. doi:10.1002/ijc.25516.
- Giannini, V., Mazzetti, S., Vignati, A., Russo, F., Bollito, E., Porpiglia, F.,  
Stasi, M., Regge, D., 2015. A fully automatic computer aided diagnosis system  
for peripheral zone prostate cancer detection using multi-parametric magnetic  
resonance imaging. Computerized Medical Imaging and Graphics 46, 219–226.  
425 doi:10.1016/j.compmedimag.2015.09.001.
- Glozzi, A., Mazzetti, S., Delsanto, P.P., Regge, D., Stasi, M., 2011. Phe-  
nomenological universalities: a novel tool for the analysis of dynamic contrast  
enhancement in magnetic resonance imaging. Physics in medicine and biology  
56, 573.
- 430 Haase, A., Frahm, J., Matthaei, D., Hancic, W., Merboldt, K.D., 1986. Flash  
imaging. rapid nmr imaging using low flip-angle pulses. Journal of Magnetic  
Resonance (1969) 67, 258–266. doi:10.1016/0022-2364(86)90433-6.

- Heilmann, M., Kiessling, F., Enderlin, M., Schad, L.R., 2006. Determination of pharmacokinetic parameters in dce mri: consequence of nonlinearity between contrast agent concentration and signal intensity. *Investigative radiology* 41, 536–543. doi:10.1097/01.rli.0000209607.99200.53.
- Hoffmann, U., Brix, G., Knopp, M.V., Heß, T., Lorenz, W.J., 1995. Pharmacokinetic mapping of the breast: a new method for dynamic mr mammography. *Magnetic resonance in medicine* 33, 506–514. doi:10.1002/mrm.1910330408.
- Huisman, H.J., Engelbrecht, M.R., Barentsz, J.O., 2001. Accurate estimation of pharmacokinetic contrast-enhanced dynamic mri parameters of the prostate. *Journal of Magnetic Resonance Imaging* 13, 607–614. doi:10.1002/jmri.1085.
- Ibanez, L., Schroeder, W., Ng, L., Cates, J., 2005. The itk software guide .
- Lemaitre, G., Dastjerdi, M.R., Massich, J., Vilanova, J.C., Walker, P.M., Freixenet, J., Meyer-Baese, A., Mériaudeau, F., Marti, R., 2016. Normalization of t2w-mri prostate images using rician a priori, in: *SPIE Medical Imaging, International Society for Optics and Photonics*. pp. 978529–978529. doi:10.1117/12.2216072.
- Lemaître, G., Martí, R., Freixenet, J., Vilanova, J.C., Walker, P.M., Meriaudeau, F., 2015. Computer-aided detection and diagnosis for prostate cancer based on mono and multi-parametric mri: A review. *Computers in biology and medicine* 60, 8–31. doi:10.1016/j.combiomed.2015.02.009.
- Litjens, G., Debats, O., Barentsz, J., Karssemeijer, N., Huisman, H., 2014. Computer-aided detection of prostate cancer in mri. *IEEE transactions on medical imaging* 33, 1083–1092. doi:10.1109/TMI.2014.2303821.
- Meng, R., Chang, S.D., Jones, E.C., Goldenberg, S.L., Kozlowski, P., 2010. Comparison between population average and experimentally measured arte-



- 460 rial input function in predicting biopsy results in prostate cancer. *Academic radiology* 17, 520–525. doi:10.1016/j.acra.2009.11.006.
- Parker, G.J., Roberts, C., Macdonald, A., Buonaccorsi, G.A., Cheung, S., Buckley, D.L., Jackson, A., Watson, Y., Davies, K., Jayson, G.C., 2006. Experimentally-derived functional form for a population-averaged high-  
465 temporal-resolution arterial input function for dynamic contrast-enhanced mri. *Magnetic resonance in medicine* 56, 993–1000. doi:10.1002/mrm.21066.
- Schabel, M.C., Parker, D.L., 2008. Uncertainty and bias in contrast concentration measurements using spoiled gradient echo pulse sequences. *Physics in medicine and biology* 53, 2345. doi:10.1088/0031-9155/53/9/010.
- 470 Shanbhag, D., Gupta, S.N., Rajamani, K., Zhu, Y., Mullick, R., 2012. A generalized methodology for detection of vascular input function with dynamic contrast enhanced perfusion data, in: *ISMRM*, p. 10.
- Sorensen, D.C., 1982. Newton’s method with a model trust region modification. *SIAM Journal on Numerical Analysis* 19, 409–426. doi:10.1137/0719026.
- 475 Tofts, P.S., Berkowitz, B., Schnall, M.D., 1995. Quantitative analysis of dynamic gd-dtpa enhancement in breast tumors using a permeability model. *Magnetic Resonance in Medicine* 33, 564–568. doi:10.1002/mrm.1910330416.
- Weinreb, J.C., Barentsz, J.O., Choyke, P.L., Cornud, F., Haider, M.A., Macura, K.J., Margolis, D., Schnall, M.D., Shtern, F., Tempany, C.M., et al., 2016. Pi-  
480 rads prostate imaging–reporting and data system: 2015, version 2. *European urology* 69, 16–40.
- Zhu, Y., Chang, M.C., Gupta, S., 2011. Automated determination of arterial input function for dce-mri of the prostate, in: *SPIE Medical Imaging, International Society for Optics and Photonics*. pp. 79630W–79630W.  
485 doi:10.1117/12.878213.